CHEMISTRY OF MATERIALS
Cite This: Chem. Mater. 2019, 31, 4685−4697
Article
pubs.acs.org/cm

Structural Diversity in Cesium Bismuth Halide Nanocrystals

Sidney E. Creutz, Hongbin Liu, Mitchell E. Kaiser, Xiaosong Li, and Daniel R. Gamelin*

Department of Chemistry, University of Washington, Seattle, Washington 98195-1700, United States

Supporting Information

ABSTRACT: Cesium bismuth halides (Cs-Bi-X) have recently been the subject of considerable attention as possible less-toxic alternatives to lead halide perovskites for luminescence and photovoltaics applications, but the full range of synthetically accessible Cs-Bi-X compositions has not been thoroughly explored, and some inconsistent results have appeared in the literature. Here, we have used a combination of hot-injection synthesis and post-synthetic anion exchange to prepare Cs-Bi-X nanocrystals with many structures and compositions, including several that have not previously been characterized. The structural and optical properties of Cs_3BiX_6 (X = Cl, Br, I) nanocrystals and $Cs_3Bi_2X_9$ (X = Cl, Br, I) nanoplatelets are reported, and interconversion of these structures between different halide compositions is demonstrated through anion exchange using trimethylsilyl halides. Notably, we find that anion exchange can be used to access structural polymorphs not readily prepared through direct synthesis. In particular, a new structural modification of $Cs_3Bi_2I_9$ has been accessed; whereas hot injection gives the previously reported "zero-dimensional" nonperovskite structure, anion exchange provides access to a "two-dimensional" layered, ordered-vacancy perovskite phase with a red-shifted absorption spectrum and distinctly different photoluminescence. Spectroscopic and computational characterization of these materials provides insight into structure/property relationships, including properties of the layered $Cs_3Bi_2I_9$ material, that may be advantageous for optoelectronic applications.

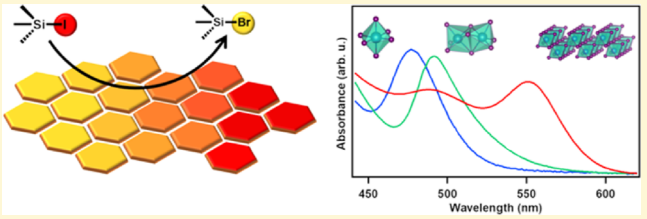

INTRODUCTION

Lead halide perovskites ($APbX_3$, X = Cl, Br, I, and A = methylammonium (MA), formamidinium, Cs) are currently being widely explored for applications in photovoltaics and, in nanocrystal form, as light emitters,[1−5] but concerns about the toxicity of lead present obstacles to their widespread application.[6] The search for lead-free perovskite analogues is, thus, a highly active area of research.[7−9] Most efforts have focused on finding lead-free materials with both structural and electronic similarities to the lead halide perovskites. Prominent candidates include other metal halide materials incorporating heavy-metal cations with an ns^2 electron configuration such as $ASnX_3$, elpasolites (i.e., double perovskites, such as Cs_2AgBiX_6), and materials based on trivalent cations such as $A_3Bi_2X_9$ and $A_3Sb_2X_9$.[10−12] Each of these classes of materials has some disadvantages, however, and none has yet come very close to matching the effectiveness of lead halide perovskites either for photovoltaics or light emission. For instance, Sn^{2+}-based materials suffer from serious stability problems due to the ease of oxidation to Sn^{4+}.[13] In addition to the need to replace Pb^{2+} with a less-toxic cation, materials with greater long-term stability under ambient conditions are sought.[14] Further work on the synthesis and understanding of this class of materials is desirable, both for the fundamental aim of exploring more thoroughly the lead-free metal halide perovskites as a class and for the practical objective of replacing lead-based semiconductors in future device technologies.

Cesium and methylammonium bismuth halides, in particular $Cs_3Bi_2X_9$ and $MA_3Bi_2X_9$, have been the subjects of several recent reports that describe their preparation as nanocrystals and as thin films and their potential application as light emitters or in solar cells.[9,15−19] Although these materials have been identified by computational screening as likely candidates for defect-tolerant semiconductors,[20] photovoltaics incorporating $Cs_3Bi_2I_9$ and $MA_3Bi_2I_9$ have reached only relatively low efficiencies. The first $A_3Bi_2I_9$ thin-film solar cells had power conversion efficiencies (PCEs) of only 0.12 and 1.09% for A = MA and Cs, respectively;[18] improvements in film morphology have since pushed their PCEs to 3.17 and 3.20%, respectively.[19,21,22] Thus, although $A_3Bi_2I_9$ films do show markedly enhanced stability compared to hybrid lead iodide perovskite films,[23,24] their PCEs to date are not yet competitive. A number of reasons for these low PCEs have been hypothesized, primarily on the basis of computational studies. Recent studies have suggested that these materials may possess problematic deep defect states that cause both the low PCEs and the poor luminescence observed in this family of materials.[25] On the other hand, low PCEs have also been attributed at least in part to a combination of high carrier effective masses, large exciton-binding energies, and poor charge-carrier mobilities, all of which stem in part from the low-dimensional $A_3Bi_2I_9$ (A = Cs, MA) crystal structures.[25−27] Additionally, these materials are believed to be indirect

Received: February 13, 2019
Revised: May 6, 2019
Published: June 17, 2019

DOI: 10.1021/acs.chemmater.9b00640
Chem. Mater. 2019, 31, 4685−4697

bandgap semiconductors, albeit with a direct bandgap only slightly higher in energy than the indirect gap.[28]

Interest in $Cs_3Bi_2X_9$ as lead-free perovskite replacements has also stimulated investigation into colloidal nanocrystals of these materials, largely with the hope that they might share the excellent emissive properties exhibited by lead halide perovskite nanocrystals.[9] Although several syntheses of Cs-Bi-X colloidal nanocrystals have been reported, discrepancies in the reported optical properties highlight the complexity of this system and warrant additional characterization.[17,29−33] The combination of Cs^+, Bi^{3+}, and halide anions (Cl^-, Br^-, I^-) can give rise to numerous different crystalline materials with varying compositions or structures, including Cs_3BiX_6 (Scheme 1A) and structural modifications of $Cs_3Bi_2X_9$ that include

Scheme 1. Structures of Cs_3BiCl_6, $Cs_3Bi_2Br_9$, and $Cs_3Bi_2I_9$ in Bulk

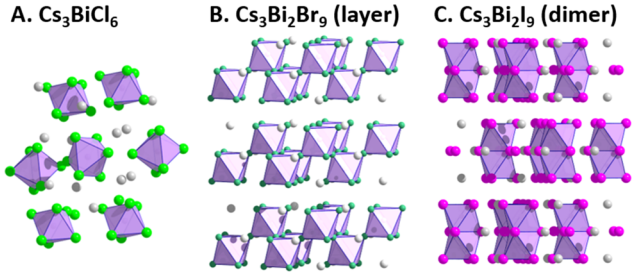

either layers of BiX_6^{3-} octahedra (X = Cl^-, Br^-) or $Bi_2X_9^{3-}$ dimers (X = I^-) (Scheme 1B,C). A systematic examination of colloidal Cs-Bi-X nanocrystals to identify and characterize the range of accessible compositions is still lacking.

In addition to the synthesis of known materials as colloidal nanocrystals, the ability of numerous halide nanocrystals to undergo facile anion-exchange reactions offers the possibility of accessing novel compositions or structural modifications that have not been accessed in bulk.[34−36] In this context, $Cs_3Bi_2I_9$ is of particular interest. As noted above, it has been suggested that one reason for the poor photovoltaic and luminescence efficiencies of $A_3Bi_2I_9$ (A = Cs, MA) may be the low electronic dimensionality of these materials, which feature isolated $Bi_2I_9^{3-}$ dimers of face-sharing octahedra interspersed with Cs^+ or MA^+ cations (Scheme 1C), resulting in large effective masses and exciton-binding energies.[26,37] In contrast, variants with other halides or other A-site cations, including $Cs_3Bi_2Br_9$ and $Rb_3Bi_2I_9$, feature a two-dimensional layered structure that is related to the perovskite structure by replacing one third of the B-site cations with vacancies (referred to as a "vacancy-ordered" or "defect" perovskite; Scheme 1B).[38,39] It has been hypothesized that this layered structure may offer more favorable charge-transport properties.[15,37,40−42] In particular, a recent computational study compared $Cs_3Bi_2I_9$ in its experimentally observed "zero-dimensional" dimer form ($P6_3/mmc$) with a hypothetical "two-dimensional" layered form ($P\bar{3}m1$) and found that the layered polymorph showed a lower bandgap (by 0.5 eV) and a higher degree of orbital delocalization at the conduction-band (CB) minimum, both potentially leading to improved performance in photovoltaic devices.[43]

A similar situation exists for the antimony-containing halide materials, $A_3Sb_2I_9$, where the comparison between the dimer and layered modifications has been more thoroughly studied. In this system, both modifications of $Cs_3Sb_2I_9$ can be accessed as thin films using different preparation methods.[44,45] The layered polymorph ($P\bar{3}m1$) has been reported to have a lower bandgap than the dimer polymorph ($P6_3/mmc$), and some studies have suggested that the layered modification can outperform the dimer modification in photovoltaic applications.[41,42,46,47] These results lend some credence to the importance of the structure in modifying the optoelectronic properties of these materials. For $Cs_3Bi_2I_9$, the analogous comparison has not yet been possible because of the lack of methods for preparing the layered modification. The layered polymorph is known in $K_3Bi_2I_9$ and $Rb_3Bi_2I_9$, however, albeit with a lower-symmetry distorted lattice ($P2_1/n$), presumably due to the smaller A-site cation size. Direct comparisons between these materials are limited, but a change in the nature of the bandgap from indirect to direct on going from the dimer structure (A = Cs) to the layered structure (A = Rb) has been noted.[39,40]

Here, we report the synthesis and characterization of colloidal nanocrystals of Cs_3BiX_6 and $Cs_3Bi_2X_9$ (X = Cl, Br, I). Access to these nanomaterials, several of which had not been previously characterized, was achieved through a combination of hot-injection synthesis and anion-exchange routes, using trimethylsilyl halide (TMSX) reagents whose utility we have recently established in this context.[48] Characterization of these nanocrystals has allowed us to begin to interrogate the influence of the composition and crystal structure of the cesium bismuth halide materials on their electronic structure and optical properties. In particular, we present evidence suggesting that a new layered modification of $Cs_3Bi_2I_9$ can be accessed using anion exchange on $Cs_3Bi_2Br_9$ nanocrystals, providing a route to previously uncharacterized lead-free perovskite analogues of potential relevance to future optoelectronic applications.

EXPERIMENTAL SECTION

General. Manipulations were carried out in ambient air except where otherwise stated. Oleylamine (70%), oleic acid (90%), octadecene (90%), anhydrous Cs(OAc) (>99.99%), anhydrous $Bi(OAc)_3$ (>99.99%), TMSBr (97%), and trimethylsilyl iodide (TMSI) (97%, with Al as a stabilizer) were purchased from Sigma-Aldrich and used as received; TMSCl (98%) was purchased from Acros Organics. Anhydrous toluene was degassed and dried by passage through a Grubbs-type solvent system[49] prior to use; hexane was dried by refluxing over sodium/benzophenone and distilled. Any other solvents and reagents were purchased from standard chemical suppliers and used as received. TMSX reagents are air-sensitive and reactive liquids; TMSBr and TMSI were manipulated in a nitrogen-filled glovebox or using Schlenk techniques, whereas TMSCl was generally handled in air without special precautions.

Characterization Methods. UV−vis absorption measurements were carried out on a Varian Cary 60 or 5000 spectrometer in 1 cm quartz cuvettes. Low-temperature photoluminescence (PL) spectra were collected with the sample deposited as a dropcast film on 1 cm quartz disks in a liquid-helium-cooled cryostat using 405 nm excitation. Emission from the sample was passed through a fiberoptic cable and monochromator, and the spectrum was collected on a liquid-nitrogen-cooled silicon charge-coupled device. Transmission electron microscopy (TEM) images were obtained on an FEI TECNAI F20 microscope operated at 200 kV; TEM samples were prepared by drop-casting dilute nanocrystal solutions onto 400 mesh carbon-coated copper grids from TED Pella, Inc. Size distributions were determined by the analysis of >200 individual nanocrystals, unless otherwise stated. For inductively coupled plasma atomic emission spectroscopy (ICP-AES), samples were dried, digested in concentrated nitric acid by sonicating overnight, and analyzed with a PerkinElmer 8300 spectrometer; concentrations were determined by

DOI: 10.1021/acs.chemmater.9b00640
Chem. Mater. 2019, 31, 4685−4697

comparison to a calibration curve constructed using a Bi^{3+} standard from Sigma-Aldrich. Nanocrystal samples were prepared for powder X-ray diffraction (PXRD) by depositing from the solution onto a silicon substrate and analyzed on a Bruker D8 Discover diffractometer using Cu Kα radiation; unless otherwise stated, a polynomial background correction was applied to the XRD data in postprocessing. XRD samples were prepared in a nitrogen glovebox and exposed to the air briefly during data collection. For energy dispersive X-ray spectroscopy (EDS) analysis, samples dropcast onto silicon substrates were coated with a ∼200-nm-thick layer of carbon; spectra were acquired in an FEI Sirion scanning electron microscope operating at 25 kV using an Oxford EDS spectrometer. Standardless quantification was used.

Synthesis of $Cs_3Bi_2X_9$ (X = Cl, Br) Nanoplatelets. Cesium acetate (48 mg, 0.25 mmol), bismuth(III) acetate (193 mg, 0.50 mmol), oleylamine (250 mg), octadecene (6 g), and oleic acid (4 g) were combined in a 50 mL three-neck round-bottom flask. The mixture was degassed and dried by stirring and heating to 120 °C under vacuum for 1 h. Then, under an N_2 atmosphere, the reaction mixture was heated to 160 °C, and 500 μL of neat TMSX (X = Cl or Br, 4 mmol) was swiftly injected; the reaction mixture immediately became cloudy and white (X = Cl) or yellow (X = Br). After 15 s, the flask was immersed in an ice-water bath and cooled to room temperature. The crude reaction mixture, which typically contains minor amounts of impurities, such as Cs_3BiX_6 nanocrystals, was decanted from the reaction flask and centrifuged for 30 min at 6000 rpm; the supernatant was then thoroughly drained from the white (X = Cl) or yellow (X = Br) precipitate. The precipitate was resuspended in a small amount of toluene (∼4 mL) and briefly sonicated before centrifuging again for 30 min. The supernatant, which typically contains Cs_3BiX_6 impurities as well as some $Cs_3Bi_2X_9$ nanocrystals, is decanted from the precipitate and discarded. The precipitate is resuspended in hexane (∼15 mL) with brief sonication and again centrifuged for 30 min. The hexane supernatant contains the desired $Cs_3Bi_2X_9$ nanoplatelets, which are decanted from the precipitate, which is discarded. The nanocrystals are stored under anhydrous conditions in an N_2 drybox; storing in ambient conditions typically results in the nanocrystals precipitating from the solution after a few days, although they can be resuspended by adding a small amount of oleic acid and oleylamine and sonicating.

Synthesis of Cs_3BiX_6 (X = Cl, Br) Nanocrystals. Cesium acetate (for X = Cl: 190 mg, 1.0 mmol; for X = Br: 95 mg, 0.5 mmol), bismuth(III) acetate (193 mg, 0.5 mmol), oleylamine (2 g), octadecene (8 g), and oleic acid (2 g) were combined in a 50 mL three-neck round-bottom flask. The mixture was degassed and dried by stirring and heating to 120 °C under vacuum for 1 h. Then, under an N_2 atmosphere, the reaction mixture was heated to 160 °C, and 380 μL of neat TMSX (X = Cl or Br, 3 mmol) was swiftly injected; the reaction mixture immediately becomes cloudy and off-white. After 15 s, the flask was immersed in an ice-water bath and cooled to room temperature. The crude reaction mixture was centrifuged for 30 min at 6000 rpm, and then the supernatant was thoroughly drained from the white or pale yellow precipitate. Toluene (∼10 mL) was added to resuspend the precipitate; typically, the precipitate can be fully resuspended with little to no insoluble material remaining. Ethyl acetate (∼10 mL) is added to precipitate the nanocrystals, and the mixture is centrifuged for 10 min. The supernatant is then decanted, and the nanocrystals resuspended in hexane (∼10 mL) and briefly centrifuged (5 min) to remove any insoluble material (typically minimal). The nanocrystals are stored under anhydrous conditions in an N_2 drybox.

Synthesis of $Cs_3Bi_2I_9$ (Dimer Modification) Nanocrystals. Cesium acetate (24 mg, 0.13 mmol), bismuth(III) acetate (97 mg, 0.50 mmol), octadecene (3 g), oleylamine (150 mg), and oleic acid (2 g) were combined in a 25 mL round-bottom three-neck flask and dried and degassed by heating and stirring at 120 °C under vacuum for 1 h. Then, the reaction mixture was heated to 160 °C under an N_2 atmosphere, and neat trimethylsilyl iodide (TMSI, 250 μL, 1.8 mmol) was swiftly injected. The reaction mixture immediately turned bright orange, and after 15 s, it was immersed in an ice-water bath and cooled to room temperature. The crude reaction mixture was centrifuged for 60 min at 6000 rpm, and then the supernatant was thoroughly drained from the orange precipitate. The precipitate was resuspended in a small amount of toluene (∼4 mL) and briefly sonicated before centrifuging again for 30 min. The supernatant is decanted from the precipitate and discarded. The precipitate is resuspended in hexane (∼15 mL) with brief sonication and again centrifuged for 10 min. The hexane supernatant contains the desired $Cs_3Bi_2I_9$ nanocrystals, which are decanted from the precipitate, which is discarded. The nanocrystals are stored under anhydrous conditions in an N_2 drybox.

General Procedure for Anion-Exchange Reactions. Essentially, the same procedure was used for all anion-exchange reactions on Cs_3BiX_6 or $Cs_3Bi_2X_9$ nanocrystals using either TMSBr (for chloride to bromide exchange) or TMSI (for bromide to iodide exchange). Anion-exchange reactions were carried out in a nitrogen glovebox. A solution of nanocrystals in toluene was prepared at a concentration of ∼1−5 mM (<0.5 mM for $Cs_3Bi_2Br_9$ to $Cs_3Bi_2I_9$ exchange). The anion-exchange reagent (TMSBr or TMSI) was added to the nanocrystals at room temperature as a 0.1 M solution in toluene. After the exchange reached completion (monitored by UV−vis absorbance), excess reagent and the TMSCl or TMSBr byproduct from the exchanged halide can be removed by drying the nanocrystals in vacuo.[48]

Density Functional Theory (DFT) Calculations. Calculations were performed with the Vienna ab initio simulation package[50,51] using a plane-wave basis set with the projector augmented wave method and Perdew−Burke−Ernzerhof exchange correlation functional.[52,53] Wavefunctions were expanded in-plane waves with an energy cutoff of 500 eV. For Cs, Bi, and I atoms, 5s5p6s, 6s6p, 5s5p valence electrons were explicitly treated, respectively. The convergence criterion in total energy was set to 10^{-4} eV. To calculate band structures, lattices were first relaxed until the Hellman−Feynman force on each atom was below 0.01 eV/Å. To sample the Brillouin zones for the layered and hexagonal structures, 6 × 6 × 5 and 6 × 6 × 2 *k*-meshes were used, respectively. The special *k*-points and the *k*-point paths used to calculate the band structures were those defined by Setyawan and Curtarolo; we interpolate 30 points between each pair of special *k*-points.[54] Effective masses were calculated based on the parabolic fitting of 6 points on each side of the conduction-band minima and valence-band (VB) maxima. Due to the significant computational cost, spin-orbit coupling is not considered in these calculations. Prior work on related heavy-metal halide perovskites suggests that higher levels of calculations (such as including spin-orbit coupling, using GW method, or hybrid functionals) can give more accurate band gaps but do not significantly alter the forms of the band structures.[55]

RESULTS AND ANALYSIS

Hot-Injection Synthesis and Structural Characterization of $Cs_3Bi_2X_9$ Nanocrystals. We first set out to develop a synthesis of well-defined $Cs_3Bi_2X_9$ (X = Cl, Br) nanocrystals. Although prior reports of $Cs_3Bi_2X_9$ nanocrystals exist, especially for X = I, synthetic routes to well-characterized samples of $Cs_3Bi_2Cl_9$ and $Cs_3Bi_2Br_9$ nanocrystals are scarce.[17] One complication in the synthesis of these materials is the fact that phases with different stoichiometries, in particular Cs_3BiX_6, can also occur, and some care must, therefore, be taken to ensure that the desired phase is accessed cleanly. Some discrepancies exist in the literature concerning the spectral properties of $Cs_3Bi_2X_9$ nanocrystals (X = Cl, Br), which may in part be due to this complication (see the Supporting Information (SI)). For this reason, we have taken care to separately synthesize and fully characterize both Cs_3BiX_6 and $Cs_3Bi_2X_9$ nanocrystals, which can both be accessed through modifications to our same synthetic conditions.

DOI: 10.1021/acs.chemmater.9b00640
Chem. Mater. 2019, 31, 4685−4697

Scheme 2. Injection of TMSX (X = Cl, Br) into a Hot Solution of Cs(OAc), $Bi(OAc)_3$, Oleylamine, and Oleic Acid (OA) in Octadecene Produces Either Cs_3BiX_6 or $Cs_3Bi_2X_9$ Nanocrystals Depending on the Ratio of Precursors and Surfactants Used

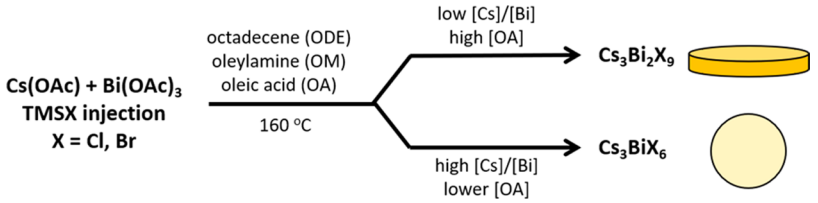

Synthetic access to Cs-Bi-X nanocrystals was achieved via a hot-injection route combining trimethylsilyl halides (TMSX) with metal acetate salts through a modification of a method that we have previously used to synthesize lead halide perovskite ($CsPbX_3$) and elpasolite (Cs_2AgBiX_6) nanocrystals.[36,48,56] Materials with different stoichiometries ($Cs_3Bi_2X_9$ or Cs_3BiX_6) could be isolated through the systematic variation of the reaction parameters and workup procedure, as detailed in the Experimental Section. Scheme 2 summarizes a typical reaction, which involved a rapid injection of neat TMSX (X = Br, Cl, or I) into a degassed solution of Cs(OAc), $Bi(OAc)_3$, oleylamine, octadecene, and oleic acid followed by rapid cooling. The desired nanocrystals could then be isolated through centrifugation and washing.

The formation of $Cs_3Bi_2X_9$ nanoplatelets (X = Cl, Br) is favored under conditions using a high [Bi]/[Cs] ratio and a large excess of oleic acid (see Experimental Section and SI for more details). This procedure results in the isolation of hexagonal nanoplatelets ~20−25 nm in diameter and ~3 nm thick; representative TEM images are shown in Figure 1A,B. The anisotropic shapes of the particles are consistent with the layered crystal structure and its hexagonal lattice. TEM imaging is complicated by the poor stability of the materials under electron beam irradiation (see SI), a property shared by the lead halide perovskites and other related materials.[30,57]

Figure 1C,D shows powder X-ray diffraction (PXRD) data collected for the $Cs_3Bi_2X_9$ nanoplatelets. In bulk, $Cs_3Bi_2Br_9$ exhibits a hexagonal crystal lattice ($P\bar{3}m1$) at room temperature with bilayers of Bi^{3+} octahedra lying perpendicular to the crystallographic c-axis; a low-temperature monoclinic form is also known with a similar connectivity.[59,60] The measured PXRD for the $Cs_3Bi_2Br_9$ nanoplatelets (Figure 1D) is in good agreement with the reported $P\bar{3}m1$ structure; the PXRD of the $Cs_3Bi_2Cl_9$ nanoplatelets (Figure 1C) is also consistent with a layered, hexagonal structure similar to its reported high-temperature *P*321 phase (see the SI for further discussion). The profile of the PXRD pattern for the nanoplatelets reflects their anisotropic shape.[61] Reflections corresponding to planes lying fully parallel to the c-axis are relatively sharp, including the prominent (*hk*0) and (*h*00) sets of reflections, whereas reflections corresponding to planes with components perpendicular to the c-axis are significantly broadened, indicating a smaller dimension in this direction. These properties, which are observed both for the $Cs_3Bi_2Br_9$ and the $Cs_3Bi_2Cl_9$ materials, are consistent with the large lateral size (~20−25 nm) and small thickness (~3 nm) of the nanoplatelets; the anisotropy of the nanocrystal shapes corresponds directly to the crystallographic anisotropy.

Figure 2 shows electronic absorption spectra collected for the $Cs_3Bi_2X_9$ nanoplatelets described above. Both spectra show a strong, sharp feature at the absorption onset, peaking at 360 nm and 430 nm for X = Cl and Br, respectively. The first

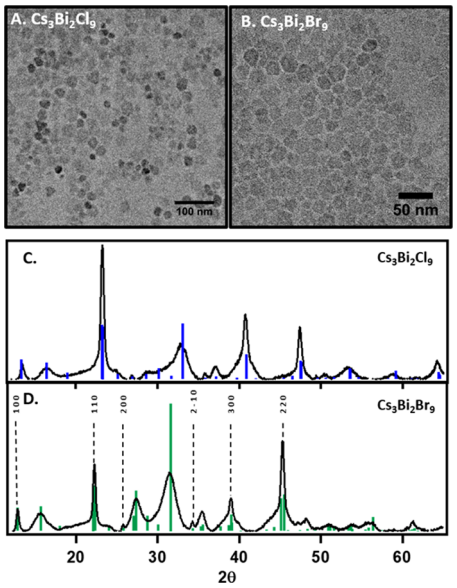

Figure 1. TEM characterization of (A, B) $Cs_3Bi_2X_9$ (X = Cl, Br) nanocrystals prepared by direct synthesis. In some materials, TEM images show black dots ~2 nm in diameter, similar to what has been observed in $CsPbX_3$ and Cs_2AgBiX_6 nanocrystals; these dots are tentatively assigned as Bi(0) particles.[58] Additional TEM images and sizing data are provided in the SI. (C) Powder XRD data for $Cs_3Bi_2Cl_9$ nanocrystals. Blue sticks correspond to an adjusted reference pattern for the high-temperature trigonal form of bulk $Cs_3Bi_2Cl_9$ (PDF 01-073-0907); lattice parameters have been adjusted to account for the different measurement temperatures (see SI). (D) Powder XRD data for $Cs_3Bi_2Br_9$ nanocrystals. Reference pattern for $Cs_3Bi_2Br_9$ (PDF 01-070-0493) is shown as green sticks. Selected sharper reflections corresponding to (*hk*0) planes are labeled (see text).

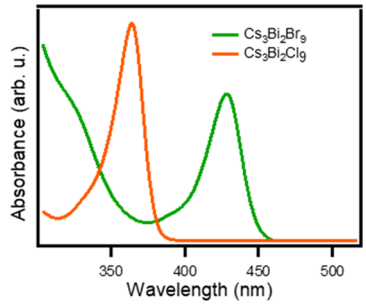

Figure 2. Absorption spectra of $Cs_3Bi_2Br_9$ (green) and $Cs_3Bi_2Cl_9$ (orange) nanoplatelets as colloidal solutions in toluene.

strong absorption feature in $Cs_3Bi_2X_9$ materials has been attributed to photoexcitation into a narrow region of the CB with a high density of states, although the possibility that this absorption has excitonic character has not been fully

DOI: 10.1021/acs.chemmater.9b00640
Chem. Mater. 2019, 31, 4685−4697

excluded.[28] In these materials, the valence-band (VB) maximum consists primarily of a mixture of halide p and bismuth 6s orbitals, whereas the CB minimum derives primarily from the bismuth 6p orbitals, giving the band-edge transition a mix of charge-transfer and bismuth 6s-6p character.[62] The absorption spectra of the nanoplatelets are generally similar to those reported for bulk crystals and thin films;[62] given the large effective masses and resulting limited delocalization of carriers in these materials,[37] significant size effects on the band gaps and spectral features due to quantum confinement are not expected.[62]

We also directly synthesized $Cs_3Bi_2I_9$ nanocrystals using a similar TMSI hot-injection procedure to facilitate the comparison to our anion-exchanged materials (vide infra). Several syntheses of $Cs_3Bi_2I_9$ nanocrystals have been reported involving a variety of methods, and our nanocrystals show similar absorption spectra to those in these prior reports, with a first absorption feature peaking at 492 nm and exhibiting a long tail to lower energies.[17,31,39] The PXRD of our material is in good agreement with the nonperovskite dimer $P6_3/mmc$ structure (PDF 01-073-0707),[63] and the TEM reveals relatively large, irregularly shaped platelet-like particles roughly 5 to 6 nm in thickness and 24.9 ± 3.7 nm in diameter. These results are discussed in more detail below.

None of the $Cs_3Bi_2X_9$ nanoplatelets we have synthesized exhibited detectable PL at room temperature; at cryogenic temperatures, we do observe some PL (vide infra). Although PL at room temperature has been reported from some samples of $Cs_3Bi_2X_9$ nanocrystals, particularly, bright blue PL in the case of X = Br, excitation spectra for these samples, when provided, differ substantially from the absorption spectra, typically showing excitation peaks at much higher energies than the absorption edge. The origin of this PL is consequently unclear.[17,32,33] Notably, similar PL has been observed from Bi^{3+} and halide-containing precursor solutions (for X = Cl, Br, I) prior to the addition of Cs^+, suggesting that in at least some cases, the reported PL may actually originate from precursors that have not been fully removed from the nanocrystal sample, rather than from the $Cs_3Bi_2X_9$ nanocrystals themselves, especially in cases where the nanocrystals were not purified prior to spectroscopic characterization.[31,33] In bulk, weak photoluminescence from $Cs_3Bi_2Br_9$ has been observed above cryogenic temperatures only in rare instances;[62] in contrast, $BiX_n^{(n-3)-}$ molecular species in solution have long been known to be luminescent at room temperature, especially for X = Cl.[64]

Synthesis and Anion Exchange of Cs_3BiX_6 Nanomaterials. In addition to $Cs_3Bi_2X_9$ nanocrystals, we have found that Cs_3BiX_6 (X = Cl, Br, I) nanocrystals can be selectively formed by the modification of the reaction conditions used above. Specifically, higher [Cs]/[Bi] ratios and less oleic acid favor the formation of Cs_3BiCl_6 over $Cs_3Bi_2Cl_9$, as summarized in Scheme 2. Rather than nanoplatelets, the Cs_3BiCl_6 nanocrystals exhibit a more isotropic shape and a smaller average dimension. The structure of Cs_3BiCl_6 reported in bulk belongs to the monoclinic $C2/c$ space group and features isolated $BiCl_6$ octahedra with no Bi-Cl-Bi bridges.[65] Figure 3A shows a representative PXRD pattern for the Cs_3BiCl_6 nanocrystals prepared here. Beyond Cs_3BiCl_6, Cs_3BiBr_6 nanocrystals could be most conveniently synthesized by anion exchange on Cs_3BiCl_6 nanocrystals using TMSBr;[48] the material synthesized by anion exchange showed the same structural (PXRD, Figure 3B) and spectroscopic (UV−vis absorption, vide infra) properties as materials synthesized directly by TMSBr injection into Cs^+ and Bi^{3+} precursors, but the directly synthesized materials suffered from a persistent CsBr impurity (see the SI). Further conversion from Cs_3BiBr_6 nanocrystals to Cs_3BiI_6 nanocrystals was also achieved by anion exchange, using TMSI as the anion-exchange reagent (Figure 3C). SEM/EDS analysis confirms that the final product corresponds to essentially a full exchange of Br^- to I^-, with <2% residual Br^-. We find that the PXRD patterns of our Cs_3BiBr_6 and Cs_3BiI_6 nanocrystals can be reasonably predicted by assuming a model isostructural to Cs_3BiCl_6 but with larger lattice constants (Figure 3A−C; see the SI for modeling). While this paper was in review, the first crystal structure determination of bulk Cs_3BiBr_6 was published; it was found to exhibit a similar zero-dimensional structure to Cs_3BiCl_6, albeit in a different space group ($Pnma$).[66] The structure of bulk Cs_3BiI_6 has not yet been reported.

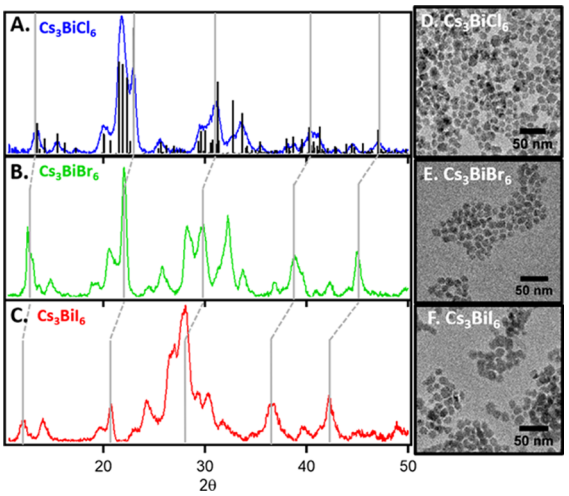

Figure 3. Powder XRD data collected for Cs_3BiCl_6 nanocrystals (A, blue) prepared by direct synthesis, and for Cs_3BiBr_6 (B, green) and Cs_3BiI_6 (C, red) nanocrystals prepared by sequential anion exchange from the Cs_3BiCl_6 nanocrystals using TMSBr and TMSI. The reference pattern for Cs_3BiCl_6 (black sticks, PDF 84-1037) is also shown; crystal structures of the other materials have not been reported. Gray lines are guides to the eye, showing shifts of selected reflections to progressively lower angles on going from Cs_3BiCl_6 to Cs_3BiBr_6 and to Cs_3BiI_6. TEM images of (D) Cs_3BiCl_6 nanocrystals prepared by direct synthesis and of (E) Cs_3BiBr_6 and (F) Cs_3BiI_6 nanocrystals prepared by anion exchange starting from the corresponding chloride sample. In some materials, TEM images show black dots ∼2 nm in diameter, similar to what has been observed in $CsPbX_3$ and Cs_2AgBiX_6 nanocrystals; these dots are tentatively assigned as Bi(0) particles.[58] Additional TEM images and sizing data are provided in the SI.

TEM images of the starting Cs_3BiCl_6 nanocrystals and the nanocrystals obtained from anion exchange (Figure 3D−F) show that the particles are still of good quality after anion exchange, with similar size, shape, and size distribution to the starting materials, suggesting that anion exchange occurs without significant restructuring or dissolution/reprecipitation. The nanocrystal size does increase slightly, from 14.2 ± 2.3 nm for Cs_3BiCl_6 to 14.5 ± 2.3 or 15.5 ± 3.1 nm for Cs_3BiBr_6 or Cs_3BiI_6, consistent with the increased lattice parameter.

The physical isolation of BiX_6^{3-} octahedra in this lattice suggests that the electronic structure of these materials will feature orbitals essentially localized on individual BiX_6^{3-} moieties, with little delocalization, narrow bands, and large carrier effective masses. Figure 4A plots absorption spectra of

DOI: 10.1021/acs.chemmater.9b00640
Chem. Mater. 2019, 31, 4685−4697

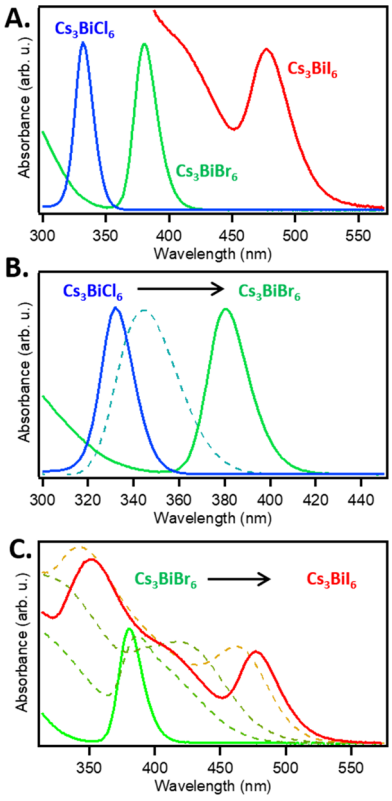

Figure 4. (A) Absorption spectra of Cs_3BiCl_6 (blue), Cs_3BiBr_6 (green), and Cs_3BiI_6 (red) nanocrystals prepared by the direct synthesis, as colloidal solutions in toluene. (B) Anion-exchange reaction of Cs_3BiCl_6 nanocrystals with TMSBr to produce Cs_3BiBr_6 nanocrystals. The reaction progresses from blue to green; the dashed curve shows the spectrum at an intermediate composition. (C) Anion-exchange reaction of Cs_3BiBr_6 nanocrystals with TMSI to produce Cs_3BiI_6 nanocrystals. The reaction progresses from green to red; the dashed lines show spectra at intermediate compositions. All absorption spectra are arbitrarily scaled.

Cs_3BiX_6 (X = Cl, Br, I) nanocrystals prepared by direct synthesis. The first absorption maxima in the spectra of the Cs_3BiX_6 nanocrystals are shifted to a significantly higher energy than those of their $Cs_3Bi_2X_9$ relatives (Figure 2); sharp, strong absorption peaks are observed at 340 and 380 nm for Cs_3BiCl_6 and Cs_3BiBr_6 nanocrystals, respectively. Figure 4B,C plots absorption spectra collected before and after anion-exchange reactions converting Cs_3BiCl_6 to Cs_3BiBr_6 and Cs_3BiBr_6 to Cs_3BiI_6, respectively. The Cs_3BiBr_6 absorption spectrum obtained after anion exchange is essentially indistinguishable from that obtained from the direct synthesis. In Cs_3BiI_6, the major absorption features are shifted to still lower energy; the first absorption peak occurs at 480 nm, with two additional peaks now discernable at higher energies (~400 and ~360 nm). In each of these spectra, the first prominent absorption peak is similar in shape and position to features reported for isolated molecular BiX_6^{3-} ions in solution. This transition is typically attributed to a Bi^{3+}-centered 6s-to-6p transition. The shift to lower energy for X = Br, I is then attributable to mixing between the s-p transition and a ligand-to-metal charge-transfer transition on the same ion.[64,67]

Anion Exchange in $Cs_3Bi_2Br_9$ Nanoplatelets to Form Layered $Cs_3Bi_2I_9$. As noted above, the layered crystal structure of the $Cs_3Bi_2Br_9$ nanocrystals differs significantly from the structure of bulk $Cs_3Bi_2I_9$, where BiI_6 moieties exist as dimers of face-sharing octahedra ($Bi_2X_9^{3-}$ units). The lack of Bi-I-Bi bridges between neighboring dimers limits electronic communication between Bi_2 dimers, and the $Bi_2X_9^{3-}$ dimers can be essentially regarded as isolated molecules. This isolation may result in limited orbital delocalization at the band edges, large exciton-binding energies, large carrier effective masses, and relatively poor carrier mobilities, and it has been speculated that this structural feature is at least in part responsible for the poor performance of photovoltaics based on $Cs_3Bi_2I_9$ or $MA_3Bi_2I_9$, which has a similar structure.[26,27,43] Access to a layered modification of $Cs_3Bi_2I_9$, isostructural to $Cs_3Bi_2Br_9$ or $Cs_3Sb_2I_9$, could help shed light on this issue by allowing the effect of structural dimensionality on the physical properties of the material to be studied; however, it has apparently not been possible to access the layered modification of $Cs_3Bi_2I_9$ through direct synthesis in nanocrystalline, bulk, or thin-film forms. Notably, three very recent reports have shown that the two-dimensional layered structure of $Cs_3Bi_2X_9$ can be maintained in alloys containing up to 2/3 I^- (e.g., $Cs_3Bi_2Br_3I_6$ and $Cs_3Bi_2Cl_3I_6$), but layered structures with higher iodide content still remain elusive.[68−70]

Given that anion exchange in metal halide nanocrystals can proceed in many cases with preservation of the cation sublattice,[36,48] we hypothesized that post-synthetic anion exchange to convert layered $Cs_3Bi_2Br_9$ nanocrystals into $Cs_3Bi_2I_9$ could yield the layered modification of $Cs_3Bi_2I_9$ as a kinetically trapped phase at room temperature. To this end, we performed anion-exchange reactions on $Cs_3Bi_2Br_9$ nanoplatelets using TMSI as the anion-exchange reagent. Treating a dilute solution of $Cs_3Bi_2Br_9$ nanoplatelets with TMSI results in a color change from yellow to orange and eventually to deep red. Figure 5 shows the evolution of the absorption spectrum

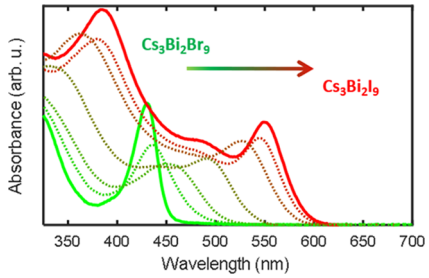

Figure 5. Absorption spectra collected during an iodide anion-exchange reaction on $Cs_3Bi_2Br_9$ nanoplatelets to produce $Cs_3Bi_2I_9$ nanoplatelets with a layered crystal structure (the reaction proceeds from green to red). All spectra correspond to the same concentration of nanocrystals.

for varying amounts of added TMSI. The prominent peak at the absorption edge shifts to lower energy over the course of the exchange and broadens significantly at intermediate points; when the exchange has reached completion, this peak has shifted to 550 nm and has a similar breadth and intensity to the analogous feature in the $Cs_3Bi_2Br_9$ starting material. Additional features are also observed at higher energies, including a prominent broad absorption band centered at 390 nm.

Figure 6 shows TEM data for the anion-exchanged material; these data, in combination with the PXRD data discussed below, confirm the successful synthesis of a novel layered modification of $Cs_3Bi_2I_9$. Starting from ~24 nm $Cs_3Bi_2Br_9$ nanoplatelets with a hexagonal shape, TEM images of the exchanged $Cs_3Bi_2I_9$ and an intermediate alloyed material (see

DOI: 10.1021/acs.chemmater.9b00640
Chem. Mater. 2019, 31, 4685−4697

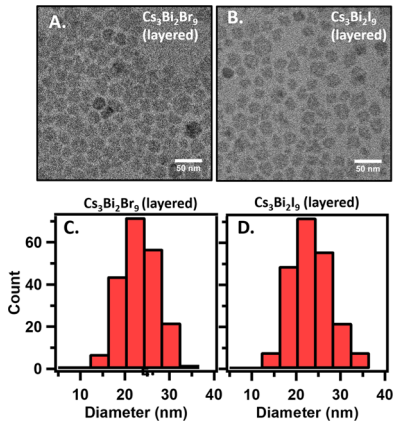

Figure 6. TEM characterization of (A) $Cs_3Bi_2Br_9$ nanoplatelets prepared by the direct synthesis and (B) $Cs_3Bi_2I_9$ nanocrystals resulting from complete anion exchange on the sample shown in panel A. (C, D) Diameter distributions for the nanocrystals shown in panels A and B. Each histogram corresponds to the measurement of at least 200 individual nanoplatelets.

SI) still show a nanoplatelet morphology with a similar size and size distribution. The size distribution measured by TEM does not change significantly; both the starting $Cs_3Bi_2Br_9$ nanoplatelets and the $Cs_3Bi_2I_9$ nanoplatelet products are 24 ± 4 nm in diameter. A small increase in size (~7%) would have been expected based on the change in the lattice parameter. The fact that such a change is not clearly observed may be consistent with a small amount of etching during the exchange.

Figure 7 summarizes PXRD data collected at various stages of the anion-exchange conversion of $Cs_3Bi_2Br_9$ to $Cs_3Bi_2I_9$. The powder XRD data from the exchanged $Cs_3Bi_2I_9$ sample are modeled well using a structure derived from the layered $P\bar{3}m1$ structure of $Cs_3Bi_2Br_9$ with expanded lattice parameters ($a = b$ = 8.58 Å; c = 10.54 Å). Importantly, the signatures of the nanoplatelet morphology in the PXRD peak widths, discussed above for $Cs_3Bi_2Br_9$, are still present in the exchanged nanocrystals, e.g., the (h00) and (hk0) reflections are distinctly sharper than other reflections, which include components along the narrow dimension of the nanoplatelets. This result supports the structural assignment. At intermediate compositions, the powder XRD data show signs of peak splitting, particularly in the (202) and (201) diffraction peaks, suggesting that the speciation of these mixed-halide materials may be more complex than simple homogeneous alloying. For instance, it may involve a lowering of the symmetry, e.g., to monoclinic, a preference for different halides in different sites or the presence of a mixture of phases with distinct compositions.[60] In fact, recent studies of $Cs_3Bi_2X_9$ alloyed crystals have shown evidence for the preferential ordering of the anions, with the larger anion (I^-) occupying predominantly terminal positions within the Bi-X layers, whereas the smaller anion (Br^- or Cl^-) preferentially occupies bridging positions.[68,69] The reference lines for the alloyed structures shown in Figure 7 assume that the $P\bar{3}m1$ symmetry and structure of $Cs_3Bi_2Br_9$ are preserved, which is only an approximation. Nevertheless, alloy halide compositions estimated from the powder XRD using Vegard's law agree with elemental compositions determined by SEM/EDS on the same samples (see the SI). Although our analysis of the nanocrystal powder XRD data cannot be considered a complete structure determination, because such determination would require

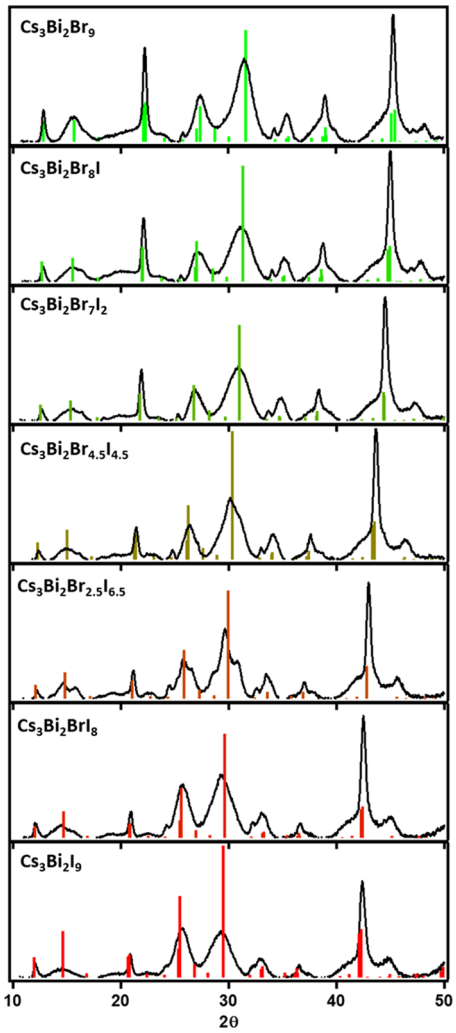

Figure 7. Powder XRD patterns for $Cs_3Bi_2(Br_{1-x}I_x)_9$ nanoplatelets at different extents of anion exchange with TMSI, proceeding from top to bottom. The reference pattern of bulk $Cs_3Bi_2Br_9$ is reproduced in the top panel (green sticks, PDF 01-070-0493); modeled XRD patterns are shown in the other panels (see text for further discussion). The compositions indicated here were estimated using Vegard's law and confirmed by SEM/EDS on a subset of the samples (see the SI).

more detailed XRD studies ideally of bulk material or single crystals, our experimental data are fully consistent with the proposed layered $P\bar{3}m1$ structure and strongly suggest the successful formation of this previously unknown layered modification of $Cs_3Bi_2I_9$.

Figure 8 provides a direct comparison of absorption spectra and the PXRD data collected for the layered $Cs_3Bi_2I_9$ nanoplatelets from anion exchange and the dimer-modification $Cs_3Bi_2I_9$ nanocrystals obtained from hot-injection synthesis. The absorption spectra (Figure 8A) are plotted in terms of absolute extinction coefficient relative to the experimental (ICP-AES) Bi^{3+} concentrations in each sample. These data indicate that the layered modification of $Cs_3Bi_2I_9$ has a larger extinction coefficient than the dimer modification throughout the visible range. The first prominent absorption peak in the dimer $Cs_3Bi_2I_9$ modification occurs at 492 nm, and a similar transition appears to be red shifted to 550 nm in the layered modification, although the broad sloping tail of the dimer $Cs_3Bi_2I_9$ absorption[39] extends almost as far as the considerably

DOI: 10.1021/acs.chemmater.9b00640
Chem. Mater. 2019, 31, 4685−4697

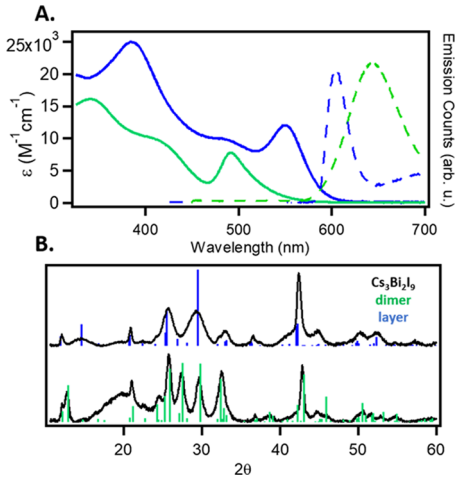

Figure 8. Comparison of the dimer and layer modifications of $Cs_3Bi_2I_9$ nanocrystals. (A) Extinction coefficient (relative to molarity of Bi^{3+} measured by ICP) for two polymorphs of $Cs_3Bi_2I_9$ (solid lines) and corresponding emission spectra (dashed lines; collected at 5 K with 405 nm excitation) for layered (blue) and dimer (green) polymorphs of $Cs_3Bi_2I_9$ synthesized by anion exchange and hot injection, respectively. Emission spectra are scaled arbitrarily. (B) Powder XRD patterns for layered (blue, top) and dimer (green, bottom) polymorphs of $Cs_3Bi_2I_9$, compared to the standard reference pattern for the dimer polymorph and the calculated pattern for the layered form.

sharper absorption edge of the layered $Cs_3Bi_2I_9$. This difference in band shape could reflect a change in the character of the band-edge transitions. The higher-energy features appear to be similarly red shifted. For example, a broader absorption feature at 420 nm in dimer $Cs_3Bi_2I_9$ appears to have shifted to 490 nm in the layered $Cs_3Bi_2I_9$, and a third higher-energy peak shifts from 340 to 390 nm and gains considerable intensity in the layered $Cs_3Bi_2I_9$ modification. The second peak in the layered $Cs_3Bi_2I_9$ nanoplatelet spectrum nearly coincides with the first peak in the dimer $Cs_3Bi_2I_9$ modification. Although it is difficult to rule out the presence of a small amount of dimer $Cs_3Bi_2I_9$ nanocrystals in the nanoplatelet sample, the powder XRD data (Figure 8B) and the uniformity of the particles observed by TEM (Figure 6) suggest that contamination is minimal, and this peak is a bona fide feature of the layered $Cs_3Bi_2I_9$ nanoplatelets.

None of the $Cs_3Bi_2I_9$ nanocrystal samples showed detectable PL at room temperature, but PL was successfully observed at cryogenic temperatures (5 K), where we find that the layered and dimer polymorphs show distinctly different emission spectra. Figure 8A plots these PL spectra. Nanocrystals of the layered polymorph show relatively sharp emission (full width at half-maximum (FWHM) ~ 85 meV) centered at 605 nm (2.05 eV), shifted from the first absorption peak by ~200 meV. Some additional, broader emission is also observed at lower energy, attributable to traps. In contrast, the nanocrystals of the dimer polymorph show a broader PL band (FWHM ~ 200 meV) at 643 nm (1.93 eV), with a larger apparent Stokes shift of ~600 meV from the first absorption peak. Similar PL has been observed in bulk and thin-film samples of dimeric $Cs_3Bi_2I_9$ and has been tentatively attributed to self-trapped excitons.[18,38] Note that both materials show slight blue shifts of the first absorption peaks with decreasing temperature, along with sharpening of the absorption features (see SI). The difference in PL spectra for the two $Cs_3Bi_2I_9$ structural polymorphs is suggestive of a change in the nature of the emissive state, possibly stemming from changes in the band structure between the two. We cannot rule out the possibility that a structural phase change occurs between room temperature and 5 K for the layered polymorph, although variable temperature PXRD shows no evidence of any dramatic phase change at least down to 139 K (see SI). The $P6_3/mmc$ dimer modification of $Cs_3Bi_2I_9$ is known to undergo a structural transition below 218 K to a similar but slightly distorted monoclinic phase.[71]

Computed Band Structure of $Cs_3Bi_2I_9$. To understand these spectroscopic differences, we examined the band structures of the two $Cs_3Bi_2I_9$ polymorphs computationally using plane-wave DFT, as described in the methods section. Geometry optimizations were carried out starting from the experimentally determined crystal structures; for both polymorphs, the computed optimized structures show slightly larger lattice parameters than the measured unit cells (see SI). Figure 9 summarizes the band structures calculated for the

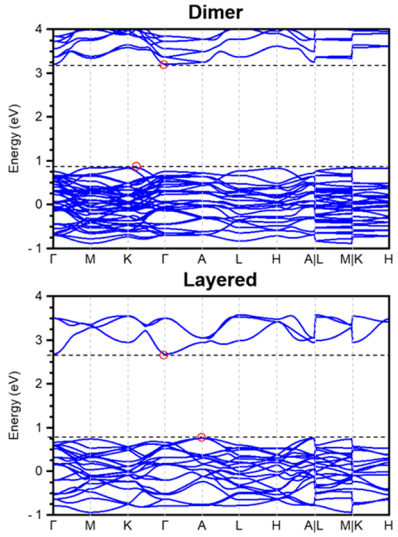

Figure 9. Calculated band structures for dimer and layered phases of $Cs_3Bi_2I_9$ (top and bottom, respectively). VB maxima and CB minima are marked by red circles.

layered $P\bar{3}m1$ and dimer $P6_3/mmc$ structures of $Cs_3Bi_2I_9$. These results are generally consistent with those from previous computational work,[40,72] but a few salient features are noteworthy.

First, the layered polymorph boasts a significantly smaller calculated bandgap than the dimer polymorph (1.9 vs 2.3 eV), in qualitative agreement with the experimental results. Inspection of the band structure diagrams suggests that this difference arises largely from the lower CB minimum in the $P\bar{3}m1$ structure. Both structures show indirect band gaps with the CB minimum at the Γ point, but for the $P6_3/mmc$ dimer structure, this minimum occurs in a flat area of the band extending between the Γ and A points, whereas for the $P\bar{3}m1$ structure, the CB minimum exhibits greater curvature and a wider band. This contrast is consistent with the expectation, discussed above, that the greater interconnectivity of the layered structure should be manifested as more dispersive bands, which could lead to better carrier mobilities. Our calculated carrier effective masses corroborate this conclusion, with a lower effective mass for the electron in both the in-plane

DOI: 10.1021/acs.chemmater.9b00640
Chem. Mater. 2019, 31, 4685−4697

and out-of-plane directions in the layered polymorph (Table 1). The VB maxima occur at A for the layered structure and between Γ and K for the dimer structure. In both cases, there are several points along the top of the VB that are fairly close in energy; the layered polymorph also shows slightly greater curvature at the VB maximum and thus a lower hole effective mass (Table 1). The carrier effective masses are larger than or comparable to values that have been previously calculated for $CsPbI_3$ (e.g., ca. $0.11m_e$ and $0.13m_e$ for the electron and hole effective masses, respectively).[73] Density of-states plots show a significant split in the CB for layered $Cs_3Bi_2I_9$ that is absent for the dimer polymorph, and that is similar to what was previously calculated for $Rb_3Bi_2I_9$, which occurs in a similar layered structure (see SI).[39]

Table 1. Calculated Effective Masses for Different Structural Polymorphs of $Cs_3Bi_2I_9$[a]

	m_e^* (‖c)	m_e^* (⊥c)	m_h^* (‖c)	m_h^* (⊥c)
layered ($P\bar{3}m1$)	$0.52m_e$[b]	$0.09m_e$	$2.7m_e$	$1.02m_e$
dimer ($P6_3/mmc$)	$1.56m_e$	$0.11m_e$	[c]	$1.14m_e$

[a]Effective masses parallel (out-of-plane) or perpendicular (in-plane) to the crystallographic *c*-axis are given. [b]m_e = electron rest mass. [c]Since the VB maximum for the dimer form lies between the K and Γ points, on an entirely in-plane path, no out-of-plane value is available from this calculation.

It is worth noting that small changes to the geometries of these materials can change the calculated locations of their VB maxima. For example, a 2% lattice contraction of the layered polymorph raises the calculated energy of the VB at the Γ point to nearly match the A point (see SI). On one hand, given the slight differences between the calculated and experimentally determined crystal structures, it cannot be stated conclusively that the location of the calculated VB maximum here accurately reflects the real system. From another perspective, this strong sensitivity to geometry suggests that the electronic characteristics of these materials may be highly sensitive to pressure effects, for example, from external sources (diamond anvil cell, epitaxial strain) or from internal sources (cation substitution), and such effects should be explored further. Overall, these computational results validate our expectation, and the available experimental evidence, that the crystal structure and even the specific lattice parameters both have a significant influence on the electronic band structures of these materials.

Concentration Dependence of Anion-Exchange Reactions. Finally, during the course of our anion-exchange experiments on $Cs_3Bi_2Br_9$ nanoplatelets, we observed that the reaction provided qualitatively different results depending on the concentrations of the reactants used. The reactions discussed above were all carried out under relatively dilute conditions (e.g., the concentration of TMSI in the reaction solution was ∼5 mM for full conversion to $Cs_3Bi_2I_9$). Under these conditions, the reactions are fairly slow, requiring several hours to reach completion, and preservation of the nanoplatelet cation sublattice selectively gives the layered modification of $Cs_3Bi_2I_9$ as the dominant product. When the reaction was run at a higher reactant concentration, however, a substantial fraction of the nanocrystals was converted to the dimer modification. Figure 10 illustrates this conversion by showing the appearance of the absorption peak at 490 nm that is characteristic of the dimer modification. This peak is observed when either the nanocrystal concentration (proportional to the Bi^{3+} concentration) and the TMSI concentration or just the TMSI concentration is increased. TEM also showed significant changes to the particle morphology associated with these spectral changes (see the SI).

A possible source of this concentration dependence could be the reaction kinetics. Although kinetic studies of nanocrystal anion exchange are sparse, a stopped-flow time-resolved study of anion exchange on $CsPbBr_3$ nanocrystals with PbX_2 identified two different kinetic regimes, a surface-limited regime and a diffusion-limited region.[74] In the surface-limited regime, the exchange of the incoming and outgoing anions at the nanocrystal surfaces is slower than the diffusion of anions within the lattice, and the nanocrystal maintains a homogeneous (alloyed) composition throughout the exchange. In the

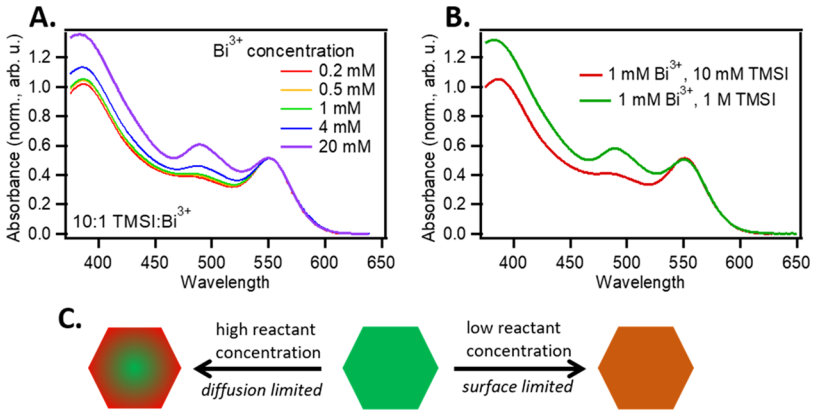

Figure 10. Effect of concentration on the anion-exchange reaction of $Cs_3Bi_2Br_9$ nanoplatelets with TMSI. (A) Absorption spectra of $Cs_3Bi_2I_9$ nanocrystals resulting from anion exchange at different reaction concentrations. The Bi^{3+} concentration for each reaction mixture was determined based on ICP measurements of a stock solution; for this size of nanoplatelets, a 1 mM concentration of Bi^{3+} corresponds to roughly a 0.2 μM concentration of nanoplatelets. TMSI was added as a 0.1 M stock solution in toluene, and the TMSI/Bi^{3+} molar ratio was fixed at 10:1 for all reactions. Absorption spectra were arbitrarily normalized to the first absorption peak. (B) Absorption spectra of $Cs_3Bi_2I_9$ nanocrystals resulting from anion exchange at different TMSI concentrations, with a constant nanocrystal concentration (1 mM in Bi^{3+}). Absorption spectra were arbitrarily normalized to the first absorption peak. (C) Proposed schematic of anion-exchange behavior in different solvated-anion concentration regimes.

DOI: 10.1021/acs.chemmater.9b00640
Chem. Mater. 2019, 31, 4685−4697

Scheme 3. Two Different Synthetic Procedures Give Rise to Different Polymorphs of $Cs_3Bi_2I_9$ as Nanoplatelets, the Dimer Polymorph and a New, Layered Polymorph

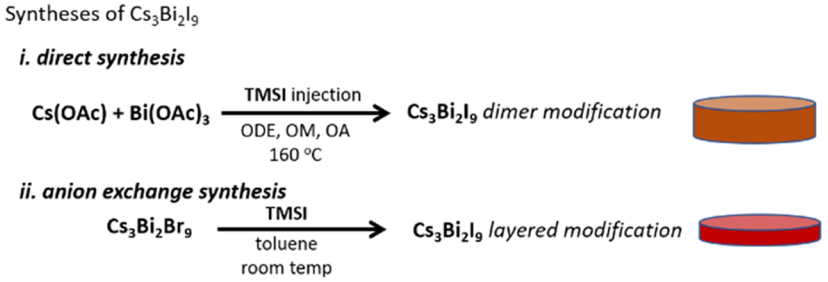

diffusion-limited regime, the exchange of anions at the surfaces is fast and the diffusion of anions inside the lattice is rate limiting. As a result, the nanocrystals have an inhomogeneous composition during the reaction, with the incoming anion concentrated near the surfaces. Koscher et al. observed the diffusion-limited behavior in bromide to iodide exchange and surface-limited behavior in bromide to chloride exchange but did not report any concentration-dependence studies.[74] A full kinetic description of this anion-exchange reaction is complex and beyond the scope of the present study, but it is likely that the rate of anion exchange at the nanocrystal surface is dependent on the reagent (TMSI) concentration, whereas anion diffusion within the nanocrystal does not depend fundamentally on the solution TMSI concentration. Therefore, it may be possible to switch between surface- and diffusion-limited regimes by changing the reagent concentration, as summarized schematically in Figure 10C. Our data would then suggest that surface-limited reactions performed at low TMSI concentrations maintain a homogeneous alloy composition throughout the reaction and better preserve the cation sublattice, whereas diffusion-limited reactions at higher TMSI concentrations are more likely to cause restructuring, perhaps as a result of greater lattice strain due to the inhomogeneous composition. The concentration dependence observed here may have implications for anion exchange in a range of halide systems and warrants further study.

CONCLUSIONS

In summary, we have developed synthetic methods that provide facile and selective access to cesium bismuth halide nanocrystals with different stoichiometries (Cs_3BiX_6 and $Cs_3Bi_2X_9$) for X = Cl, Br, and I, some of which had not been previously reported as nanocrystals or in any form. We have additionally provided structural and spectroscopic characterization of these materials that should prove useful for distinguishing among the manifold structures and compositions that can result from similar synthetic conditions. Although we have not yet explored variants with other A-site cations, it is likely that the closely related methylammonium bismuth halides share a similar structural and compositional diversity.

We have further shown that post-synthetic anion-exchange reactions can be used to tune the halide compositions in these nanocrystals, providing access to structural modifications that are difficult or perhaps impossible to synthesize directly. Most notably, we showed that a layered structural modification of $Cs_3Bi_2I_9$ can be accessed by anion exchange on $Cs_3Bi_2Br_9$ nanoplatelets. Although the previously reported nonperovskite ($P6_3/mmc$) phase that is accessed through the direct synthesis of $Cs_3Bi_2I_9$ features isolated $Bi_2I_9^{3-}$ bioctahedra, anion exchange has allowed us to access a layered ordered-vacancy perovskite phase of $Cs_3Bi_2I_9$ that has not previously been reported. The ability to access distinct structural modifications with the same $Cs_3Bi_2I_9$ composition depending on the synthesis route is summarized in Scheme 3.

Spectroscopic and computational characterization of both $Cs_3Bi_2I_9$ modifications indicate significant differences in their electronic structures that are consistent with greater band dispersion in the new two-dimensional $Cs_3Bi_2I_9$ structure formed by anion exchange than in the dimer modification formed by direct synthesis. These results indicate a strong sensitivity of the electronic properties of these materials to structural variation and suggest potential routes for tuning those electronic properties based on chemical or physical perturbations.

Overall, this work highlights the utility of anion-exchange reactivity in nanocrystals for accessing new and otherwise inaccessible electronic materials. Given the facile anion exchange generally displayed by similar classes of ionic halide materials, we anticipate that similar methods should allow the extension of these chemistries to polycrystalline thin films as well.[48] This strategy can be particularly powerful in the search for lead-free perovskite analogues for optoelectronics applications.

ASSOCIATED CONTENT

Supporting Information

The Supporting Information is available free of charge on the ACS Publications website at DOI: 10.1021/acs.chemmater.9b00640.

Additional nanocrystal characterization data, including TEM images, size distributions, PXRD, absorbance spectra, and SEM/EDS data; effect of varying reaction conditions; further PXRD analysis and modeling; variable temperature absorbance and PL spectra and PXRD data; additional computational results (PDF)

AUTHOR INFORMATION

Corresponding Author

*E-mail: gamelin@chem.washington.edu.

ORCID

Sidney E. Creutz: 0000-0003-4440-5336
Hongbin Liu: 0000-0001-9011-1182
Xiaosong Li: 0000-0001-7341-6240
Daniel R. Gamelin: 0000-0003-2888-9916

Notes

The authors declare no competing financial interest.

DOI: 10.1021/acs.chemmater.9b00640
Chem. Mater. 2019, 31, 4685−4697

■ ACKNOWLEDGMENTS

This research was supported by the U.S. National Science Foundation (NSF) through the UW Molecular Engineering Materials Center, a Materials Research Science and Engineering Center (DMR-1719797). Additional support through DMR-1807394 to D.R.G. and CHE-1565520 to X.L. is gratefully acknowledged. Part of this work was conducted at the Molecular Analysis Facility, a National Nanotechnology Coordinated Infrastructure site at UW that is supported in part by the NSF (grant ECC-1542101), UW, the Molecular Engineering & Sciences Institute, the Clean Energy Institute, and the National Institutes of Health. This research was supported by an appointment to the Intelligence Community Postdoctoral Research Fellowship Program at UW, administered by Oak Ridge Institute for Science and Education through an interagency agreement between the U.S. Department of Energy and the Office of the Director of National Intelligence (S.E.C.). This work was facilitated though the use of advanced computational, storage, and networking infrastructure provided by the Hyak supercomputer system funded by the STF at the University of Washington and the National Science Foundation (MRI-1624430). Michael C. De Siena is thanked for assistance with low-temperature photoluminescence and absorption measurements.

■ REFERENCES

(1) Snaith, H. J. Present status and future prospects of perovskite photovoltaics. *Nat. Mater.* **2018**, *17*, 372−376.
(2) Akkerman, Q. A.; Rainò, G.; Kovalenko, M. V.; Manna, L. Genesis, challenges and opportunities for colloidal lead halide perovskite nanocrystals. *Nat. Mater.* **2018**, *17*, 394−405.
(3) Kovalenko, M. V.; Protesescu, L.; Bodnarchuk, M. I. Properties and potential optoelectronic applications of lead halide perovskite nanocrystals. *Science* **2017**, *358*, 745−750.
(4) Correa-Baena, J.-P.; Saliba, M.; Buonassisi, T.; Grätzel, M.; Abate, A.; Tress, W.; Hagfeldt, A. Promises and challenges of perovskite solar cells. *Science* **2017**, *358*, 739−744.
(5) Grätzel, M. The light and shade of perovskite solar cells. *Nat. Mater.* **2014**, *13*, 838−842.
(6) Babayigit, A.; Ethirajan, A.; Muller, M.; Conings, B. Toxicity of organometal halide perovskite solar cells. *Nat. Mater.* **2016**, *15*, 247−251.
(7) Shi, Z.; Guo, J.; Chen, Y.; Li, Q.; Pan, Y.; Zhang, H.; Xia, Y.; Huang, W. Lead-Free Organic−Inorganic Hybrid Perovskites for Photovoltaic Applications: Recent Advances and Perspectives. *Adv. Mater.* **2017**, *29*, No. 1605005.
(8) Chatterjee, S.; Pal, A. J. Influence of metal substitution on hybrid halide perovskites: toward lead-free perovskite solar cells. *J. Mater. Chem. A* **2018**, *6*, 3793−3823.
(9) Sun, J.; Yang, J.; Lee, J. I.; Cho, J. H.; Kang, M. S. Lead-Free Perovskite Nanocrystals for Light-Emitting Devices. *J. Phys. Chem. Lett.* **2018**, *9*, 1573−1583.
(10) Giustino, F.; Snaith, H. J. Toward Lead-Free Perovskite Solar Cells. *ACS Energy Lett* **2016**, *1*, 1233−1240.
(11) Hoefler, S. F.; Trimmel, G.; Rath, T. Progress on lead-free metal halide perovskites for photovoltaic applications: a review. *Monatsh. Chem.* **2017**, *148*, 795−826.
(12) Lyu, M.; Yun, J.-H.; Chen, P.; Hao, M.; Wang, L. Addressing Toxicity of Lead: Progress and Applications of Low-Toxic Metal Halide Perovskites and Their Derivatives. *Adv. Energy Mater.* **2017**, *7*, No. 1602512.
(13) Noel, N. K.; Stranks, S. D.; Abate, A.; Wehrenfennig, C.; Guarnera, S.; Haghighirad, A.-A.; Sadhanala, A.; Eperon, G. E.; Pathak, S. K.; Johnston, M. B.; Petrozza, A.; Herz, L. M.; Snaith, H. J. Lead-free organic−inorganic tin halide perovskites for photovoltaic applications. *Energy Environ. Sci.* **2014**, *7*, 3061−3068.
(14) Ono, L. K.; Qi, Y.; Liu, S. Progress toward Stable Lead Halide Perovskite Solar Cells. *Joule* **2018**, *2*, 1961−1990.
(15) Li, M.-Q.; Hu, Y.-Q.; Bi, L.-Y.; Zhang, H.-L.; Wang, Y.; Zheng, Y.-Z. Structure Tunable Organic−Inorganic Bismuth Halides for an Enhanced Two-Dimensional Lead-Free Light-Harvesting Material. *Chem. Mater.* **2017**, *29*, 5463−5467.
(16) Leng, M.; Chen, Z.; Yang, Y.; Li, Z.; Zeng, K.; Li, K.; Niu, G.; He, Y.; Zhou, Q.; Tang, J. Lead-Free, Blue Emitting Bismuth Halide Perovskite Quantum Dots. *Angew. Chem., Int. Ed.* **2017**, *55*, 15012−15016.
(17) Yang, B.; Chen, J.; Hong, F.; Mao, X.; Zheng, K.; Yang, S.; Li, Y.; Pullerits, T.; Deng, W.; Han, K. Lead-Free, Air-Stable All-Inorganic Cesium Bismuth Halide Perovskite Nanocrystals. *Angew. Chem., Int. Ed.* **2017**, *56*, 12471−12475.
(18) Park, B.-W.; Philippe, B.; Zhang, X.; Rensmo, H.; Boschloo, G.; Johansson, E. M. J. Bismuth Based Hybrid Perovskites $A_3Bi_2I_9$ (A: Methylammonium or Cesium) for Solar Cell Application. *Adv. Mater.* **2018**, *27*, 6806−6813.
(19) Bai, F.; Hu, Y.; Hu, Y.; Qiu, T.; Miao, X.; Zhang, S. Lead-free, air-stable ultrathin $Cs_3Bi_2I_9$ perovskite nanosheets for solar cells. *Sol. Energy Mater. Sol. Cells* **2018**, *184*, 15−21.
(20) Brandt, R. E.; Stavanovic, V.; Ginley, D. S.; Buanoassisi, T. Identifying defect-tolerant semiconductors with high minority-carrier lifetimes: beyond hybrid lead halide perovskites. *MRS Commun.* **2018**, *5*, 265−275.
(21) Zhang, Z.; Li, X.; Xia, X.; Wang, Z.; Huang, Z.; Lei, B.; Gao, Y. High-Quality $(CH_3NH_3)_3Bi_2I_9$ Film-Based Solar Cells: Pushing Efficiency up to 1.64%. *J. Phys. Chem. Lett.* **2017**, *8*, 4300−4307.
(22) Jain, S. M.; Phuyal, D.; Davies, M. L.; Li, M.; Philippe, B.; De Castro, C.; Qiu, Z.; Kim, J.; Watson, T.; Tsoi, W. C.; Karis, O.; Rensmo, H.; Boschloo, G.; Edvinsson, T.; Durrant, J. R. An effective approach of vapour assisted morphological tailoring for reducing metal defect sites in lead-free, $(CH_3NH_3)_3Bi_2I_9$ bismuth-based perovskite solar cells for improved performance and long-term stability. *Nano Energy* **2018**, *49*, 614−624.
(23) Lyu, M.; Yun, J.-H.; Cai, M.; Jiao, Y.; Bernhardt, P. V.; Zhang, M.; Wang, Q.; Du, A.; Wang, H.; Liu, G.; Wang, L. Organic−inorganic bismuth(III)-based material: A lead-free, air-stable and solution-processable light-absorber beyond organolead perovskites. *Nano Res.* **2016**, *9*, 692−702.
(24) Hoye, R. L. Z.; Brandt, R. E.; Osherov, A.; Stavanovic, V.; Stranks, S. D.; Wilson, M. W. B.; Kim, H.; Akey, A. J.; Perkins, J. D.; Kurchin, R. C.; Poindexter, J. R.; Wang, E. N.; Bawendi, M. G.; Bulovic, V.; Buonassisi, T. Methylammonium Bismuth Iodide as a Lead-Free, Stable Hybrid Organic−Inorganic Solar Absorber. *Chem. - Eur. J.* **2018**, *22*, 2605−2610.
(25) Ghosh, B.; Chakraborty, S.; Wei, H.; Guet, C.; Li, S.; Mhaisalkar, S.; Mathews, N. Poor Photovoltaic Performance of $Cs_3Bi_2I_9$: An Insight through First-Principles Calculations. *J. Phys. Chem. C* **2017**, *121*, 17062−17067.
(26) Xiao, Z.; Meng, W.; Wang, J.; Mitzi, D. B.; Yan, Y. Searching for promising new perovskite-based photovoltaic absorbers: the importance of electronic dimensionality. *Mater. Horiz.* **2016**, *4*, 206−216.
(27) Ghosh, B.; Wu, B.; Mulmudi, H. K.; Guet, C.; Weber, K.; Sum, T. C.; Mhaisalkar, S. G.; Mathews, N. Limitations of $Cs_3Bi_2I_9$ as lead-free photovoltaic absorber materials. *ACS Appl. Mater. Interfaces* **2018**, *10*, 35000−35007.
(28) Pazoki, M.; Johansson, M. B.; Zhu, H.; Broqvist, P.; Edvinsson, T.; Boschloo, G.; Johansson, E. M. J. Bismuth Iodide Perovskite Materials for Solar Cell Applications: Electronic Structure, Optical Transitions, and Directional Charge Transport. *J. Phys. Chem. C* **2016**, *120*, 29039−29046.
(29) Zhang, Y.; Yin, J.; Parida, M. R.; Ahmed, G. H.; Pan, J.; Bakr, O. M.; Brédas, J.-L.; Mohammed, O. F. Direct-Indirect Nature of the Bandgap in Lead-Free Perovskite Nanocrystals. *J. Phys. Chem. Lett.* **2017**, *8*, 3173−3177.
(30) Pal, J.; Manna, S.; Mondal, A.; Das, S.; Adarsh, K. V.; Nag, A. Colloidal Synthesis and Photophysics of $M_3Sb_2I_9$ (M=Cs and Rb)

DOI: 10.1021/acs.chemmater.9b00640
Chem. Mater. 2019, 31, 4685−4697

Nanocrystals: Lead-Free Perovskites. *Angew. Chem., Int. Ed.* **2017**, *56*, 14187−14191.
(31) Nelson, R. D.; Santra, K.; Wang, Y.; Hadi, A.; Petrich, J. W.; Panthani, M. G. Synthesis and optical properties of ordered-vacancy perovskite cesium bismuth halide nanocrystals. *Chem. Commun.* **2018**, *54*, 3640−3643.
(32) Leng, M.; Yang, Y.; Zeng, K.; Chen, Z.; Tan, Z.; Li, S.; Li, J.; Xu, B.; Li, D.; Hautzinger, M. P.; Fu, Y.; Zhai, T.; Xu, L.; Niu, G.; Jin, S.; Tang, J. All-Inorganic Bismuth-Based Perovskite Quantum Dots with Bright Blue Photoluminescence and Excellent Stability. *Adv. Funct. Mater.* **2018**, *28*, No. 1704446.
(33) Lou, Y.; Fang, M.; Chen, J.; Zhao, Y. Formation of highly luminescent cesium bismuth halide perovskite quantum dots tuned by anion exchange. *Chem. Commun.* **2018**, *54*, 3779−3782.
(34) Akkerman, Q. A.; D'Innocenzo, V.; Accornero, S.; Scarpellini, A.; Petrozza, A.; Prato, M.; Manna, L. Tuning the Optical Properties of Cesium Lead Halide Perovskite Nanocrystals by Anion Exchange Reactions. *J. Am. Chem. Soc.* **2015**, *137*, 10276−10281.
(35) Nedelcu, G.; Protesescu, L.; Yakunin, S.; Bodnarchuk, M. I.; Grotevent, M. J.; Kovalenko, M. V. Fast Anion-Exchange in Highly Luminescent Nanocrystals of Cesium Lead Halide Perovskites ($CsPbX_3$, X = Cl, Br, I). *Nano Lett.* **2015**, *15*, 5635−5640.
(36) Creutz, S. E.; Crites, E. N.; Siena, M. C. D.; Gamelin, D. R. Colloidal Nanocrystals of Lead-Free Double-Perovskite (Elpasolite) Semiconductors: Synthesis and Anion Exchange To Access New Materials. *Nano Lett.* **2018**, *18*, 1118−1123.
(37) McCall, K. M.; Liu, Z.; Trimarchi, G.; Stoumpos, C. C.; Lin, W.; He, Y.; Hadar, I.; Kanatzidis, M. G.; Wessels, B. W. α-Particle Detection and Charge Transport Characteristics in the $A_3M_2I_9$ Defect Perovskites (A = Cs, Rb; M = Bi, Sb). *ACS Photonics* **2018**, *5*, 3748−3762.
(38) McCall, K. M.; Stoumpos, C. C.; Kostina, S. S.; Kanatzidis, M. G.; Wessels, B. W. Strong Electron−Phonon Coupling and Self-Trapped Excitons in the Defect Halide Perovskites $A_3M_2I_9$ (A = Cs, Rb; M = Bi, Sb). *Chem. Mater.* **2017**, *29*, 4129−4145.
(39) Pal, J.; Bhunia, A.; Chakraborty, S.; Manna, S.; Das, S.; Dewan, A.; Datta, S.; Nag, A. Synthesis and Optical Properties of Colloidal $M_3Bi_2I_9$ (M = Cs, Rb) Perovskite Nanocrystals. *J. Phys. Chem. C* **2018**, *122*, 10643−10649.
(40) Lehner, A. J.; Fabini, D. H.; Evans, H. A.; Hébert, C.-A.; Smock, S. R.; Hu, J.; Wang, H.; Zwanziger, J. W.; Chabinyc, M. L.; Seshadri, R. Crystal and Electronic Structures of Complex Bismuth Iodides $A_3Bi_2I_9$ (A = K, Rb, Cs) Related to Perovskite: Aiding the Rational Design of Photovoltaics. *Chem. Mater.* **2015**, *27*, 7137−7148.
(41) Harikesh, P. C.; Mulmudi, H. K.; Ghosh, B.; Goh, T. W.; Teng, Y. T.; Thirumal, K.; Lockrey, M.; Weber, K.; Koh, T. M.; Li, S.; Mhaisalkar, S.; Mathews, N. Rb as an Alternative Cation for Templating Inorganic Lead-Free Perovskites for Solution Processed Photovoltaics. *Chem. Mater.* **2016**, *26*, 7496−7504.
(42) Correa-Baena, J.-P.; Nienhaus, L.; Kurchin, R. C.; Shin, S. S.; Wieghold, S.; Hartono, N. T. P.; Layurova, M.; Klein, N. D.; Poindexter, J. R.; Polizzotti, A.; Sun, S.; Bawendi, M. G.; Buonassisi, T. A-Site Cation in Inorganic $A_3Sb_2I_9$ Perovskite Influences Structural Dimensionality, Exciton Binding Energy, and Solar Cell Performance. *Chem. Mater.* **2018**, *30*, 3734−3742.
(43) Hong, K.-H.; Kim, J.; Debbichi, L.; Kim, H.; Im, S. H. Band Gap Engineering of Cs3Bi2I9 Perovskites with Trivalent Atoms Using a Dual Metal Cation. *J. Phys. Chem. C* **2017**, *121*, 969−974.
(44) Yamada, K.; Sera, H.; Sawada, S.; Tada, H.; Okuda, T.; Tanaka, H. Reconstructive Phase Transformation and Kinetics of $Cs_3Sb_2I_9$ by Means of Rietveld Analysis of X-Ray Diffraction and 127I NQR. *J. Solid State Chem.* **1997**, *134*, 319−325.
(45) Saparov, B.; Hong, F.; Sun, J.-P.; Duan, H.-S.; Meng, W.; Cameron, S.; Hill, I. G.; Yan, Y.; Mitzi, D. B. Thin-Film Preparation and Characterization of $Cs_3Sb_2I_9$: A Lead-Free Layered Perovskite Semiconductor. *Chem. Mater.* **2015**, *27*, 5622−5632.
(46) Jiang, F.; Yang, D.; Jiang, Y.; Liu, T.; Zhao, X.; Ming, Y.; Luo, B.; Qin, F.; Fan, J.; Han, H.; Zhang, L.; Zhou, Y. Chlorine-Incorporation-Induced Formation of the Layered Phase for Antimony-Based Lead-Free Perovskite Solar Cells. *J. Am. Chem. Soc.* **2018**, *140*, 1019−1027.
(47) Singh, A.; Boopathi, K. M.; Mohapatra, A.; Chen, Y. F.; Li, G.; Chu, C. W. Photovoltaic Performance of Vapor-Assisted Solution-Processed Layer Polymorph of $Cs_3Sb_2I_9$. *ACS Appl. Mater. Interfaces* **2018**, *10*, 2566−2573.
(48) Creutz, S. E.; Crites, E. N.; Siena, M. C. D.; Gamelin, D. R. Anion Exchange in Cesium Lead Halide Perovskite Nanocrystals and Thin Films Using Trimethylsilyl Halide Reagents. *Chem. Mater.* **2018**, *30*, 4887−4891.
(49) Pangborn, A. B.; Giardello, M. A.; Grubbs, R. H.; Rosen, R. K.; Timmers, F. J. Safe and Convenient Procedure for Solvent Purification. *Organometallics* **1996**, *15*, 1518−1520.
(50) Kresse, G.; Furthmüller, J. Efficiency of ab-initio total energy calculations for metals and semiconductors using a plane-wave basis set. *Comput. Mater. Sci.* **1996**, *6*, 15−50.
(51) Kresse, G.; Furthmuller, J. Efficient iterative schemes for ab initio total-energy calculations using a plane-wave basis set. *Phys. Rev. B* **1996**, *54*, 11169−11186.
(52) Blöchl, P. E. Projector augmented-wave method. *Phys. Rev. B* **1994**, *50*, 17953−17979.
(53) Perdew, J. P.; Burke, K.; Ernzerhof, M. Generalized gradient approximation made Simple. *Phys. Rev. Lett.* **1996**, *77*, 3865−3868.
(54) Setyawan, W.; Curtarolo, S. High-throughput electronic band structure calculations: Challenges and tools. *Comput. Mater. Sci.* **2010**, *49*, 299−312.
(55) Becker, M. A.; Vaxenburg, R.; Nedelcu, G.; Sercel, P. C.; Shabaev, A.; Mehl, M. J.; Michopoulos, J. G.; Lambrakos, S. G.; Bernstein, N.; Lyons, J. L.; Stöferle, T.; Mahrt, R. F.; Kovalenko, M. V.; Norris, D. J.; Rainò, G.; Efros, A. L. Bright triplet excitons in caesium lead halide perovskites. *Nature* **2018**, *553*, 189−193.
(56) Milstein, T.; Kroupa, D.; Gamelin, D. R. Picosecond quantum cutting generates photoluminescence quantum yields over 100% in ytterbium-doped $CsPbCl_3$ nanocrystals. *Nano Lett.* **2018**, *18*, 3792−3799.
(57) Dang, Z.; Shamsi, J.; Palazon, F.; Imran, M.; Akkerman, Q. A.; Park, S.; Bertoni, G.; Prato, M.; Brescia, R.; Manna, L. In Situ Transmission Electron Microscopy Study of Electron Beam-Induced Transformations in Colloidal Cesium Lead Halide Perovskite Nanocrystals. *ACS Nano* **2017**, *11*, 2124−2132.
(58) Kim, S. H.; Choi, Y.-S.; Kang, K.; Yang, S. I. Controlled growth of bismuth nanoparticles by electron beam irradiation in TEM. *J. Alloys Compd.* **2007**, *427*, 330−332.
(59) Lazarini, F. Caesium enneabromodibismuthate(III). *Acta Crystallogr., Sect. B: Struct. Sci.* **1977**, *33*, 2961−2964.
(60) Aleksandrova, I. P.; Burriel, R.; Bartolome, J.; Bagautdinov, B. S.; Blasco, J.; Sukhovsky, A. A.; Torres, J. M.; Vasiljev, A. D.; Solovjev, L. A. Low-Temperature Phase Transitions in the Trigonal Modification of $Cs_3Bi_2Br_9$ and $Cs_3Sb_2I_9$. *Phase Trans.* **2002**, *75*, 607−620.
(61) Bertaut, E. F. Raies de Debye-Scherrer et Repartition des Dimensions des Domaines de Bragg dans les Poudres Polycristallines. *Acta. Cryst.* **1950**, *3*, 14−18.
(62) Bass, K. K.; Estergreen, L.; Savory, C. N.; Buckeridge, J.; Scanlon, D. O.; Djurovich, P. I.; Bradforth, S. E.; Thompson, M. E.; Melot, B. C. Vibronic Structure in Room Temperature Photoluminescence of the Halide Perovskite $Cs_3Bi_2Br_9$. *Inorg. Chem.* **2016**, *56*, 42−45.
(63) Lindqvist, O.; et al. The Crystal Structure of Cesium Bismuth Iodide, $Cs_3Bi_2I_9$. *Acta Chem. Scand.* **1968**, *22*, 2943−2952.
(64) Nikol, H.; Vogler, A. Photoluminescence of antimony(III) and bismuth(III) chloride complexes in solution. *J. Am. Chem. Soc.* **2002**, *113*, 8988−8990.
(65) Benachenhou, F.; Mairesse, G.; Nowogrocki, G.; Thomas, D. Structural studies of Cs-K-Bi mixed chlorides relation to the crystal structures of A_2BMX_6, A_3MX_6, and A_2MX_6. *J. Solid State Chem.* **1986**, *65*, 13−26.
(66) Tang, Y.; Liang, M.; Chang, B.; Sun, H.; Zheng, K.; Pullerits, T.; Chi, Q. Lead-free double halide perovskite Cs_3BiBr_6 with well-

DOI: 10.1021/acs.chemmater.9b00640
Chem. Mater. 2019, 31, 4685−4697

defined crystal structure and high thermal stability for optoelectronics. *J. Mater. Chem. C* **2019**, *7*, 3369−3374.
(67) Oldenburg, K.; Vogler, A. Electronic Spectra and Photochemistry of Tin(II), Lead(II), Antimony(III), and Bismuth(III) Bromide Complexes in Solution. *Z. Naturforsch., B* **2018**, *48*, 1519−1523.
(68) Hodgkins, T. L.; Savory, C. N.; Bass, K. K.; Seckman, B. L.; Scanlon, D. O.; Djurovich, P. I.; Thompson, M. E.; Melot, B. C. Anionic order and band gap engineering in vacancy ordered triple perovskites. *Chem. Commun.* **2019**, *55*, 3164−3167.
(69) McCall, K. M.; Stoumpos, C. C.; Kontsevoi, O. Y.; Alexander, G. C. B.; Wessels, B. W.; Kanatzidis, M. G. From 0D $Cs_3Bi_2I_9$ to 2D $Cs_3Bi_2I_6Cl_3$: Dimensional Expansion Induces a Direct Band Gap but Enhances Electron−Phonon Coupling. *Chem. Mater.* **2019**, *31*, 2644−2650.
(70) Yu, B.-B.; Liao, M.; Yang, J.; Chen, W.; Zhu, Y.; Zhang, X.; Duan, T.; Yao, W.; Wei, S.-H.; He, Z. Alloy-induced phase transition and enhanced photovoltaic performance: the case of $Cs_3Bi_2I_{9-x}Br_x$ perovskite solar cells. *J. Mater. Chem. A* **2019**, *7*, 8818−8825.
(71) Arakcheeva, A. V.; Bonin, M.; Chapuis, G.; Zaitsev, A. I. The phases of $Cs_3Bi_2I_9$ between RT and 190 K. *Z. Kristallogr. - Cryst. Mater.* **1999**, *214*, 279−283.
(72) Du, K.-Z.; Meng, W.; Wang, X.; Yan, Y.; Mitzi, D. B. Bandgap Engineering of Lead-Free Double Perovskite $Cs_2AgBiBr_6$ through Trivalent Metal Alloying. *Angew. Chem., Int. Ed.* **2017**, *56*, 8158−8162.
(73) Protesescu, L.; Yakunin, S.; Bodnarchuk, M. I.; Krieg, F.; Caputo, R.; Hendon, C. H.; Yang, R. X.; Walsh, A.; Kovalenko, M. V. Nanocrystals of Cesium Lead Halide Perovskites ($CsPbX_3$, X = Cl, Br, and I): Novel Optoelectronic Materials Showing Bright Emission with Wide Color Gamut. *Nano Lett.* **2015**, *15*, 3692−3696.
(74) Koscher, B. A.; Bronstein, N. D.; Olshansky, J. H.; Bekenstein, Y.; Alivisatos, A. P. Surface- vs Diffusion-Limited Mechanisms of Anion Exchange in $CsPbBr_3$ Nanocrystal Cubes Revealed through Kinetic Studies. *J. Am. Chem. Soc.* **2016**, *138*, 12065−12068.

DOI: 10.1021/acs.chemmater.9b00640
Chem. Mater. 2019, 31, 4685−4697